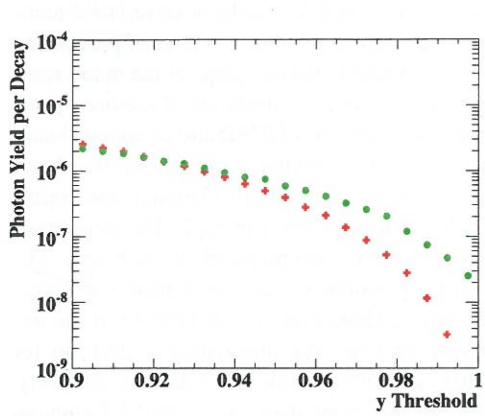

Figure 22 The RMD (red crosses) and AIF (green circles) γ-ray background spectra around the signal region in the MEG detector estimated by MC simulations.

most 4–6%. The pile-up rejection methods ~~are~~ already have been discussed in Sect. 3.1.3. The cosmic ray events are rejected by using topological cuts based on the deposited charge ratio of the inner to outer face and the reconstructed depth (w) because these events mostly come from the outer face of the LXe detector while signal events are expected from the inner face. After applying these cuts, γ-ray background spectra are directly measured from the time side-band data, and the measured shape is used ~~for~~ in the physics analysis.

4.3.2 Accidental background

Editor's comments:
Section coordinator: Wataru

The accidental overlap between a positron with energy close to the kinematic edge of the Michel decay and an energetic γ-ray from RMD or positron AIF is a leading source of the background for the $\mu^+ \to e^+\gamma$ search in the MEG experiment.

The effective branching ratio of the accidental background, defined by the background rate normali~~s~~zed to the muon stopping rate, can be approximately expressed by [27]

$$B_{acc} \propto R_\mu \delta E_e (\delta E_\gamma)^2 \delta t_{e\gamma} \delta\theta_{e\gamma} \delta\phi_{e\gamma},$$

where R_μ is the muon stopping rate and δx is the width of the signal region normally defined by the detector resolution for the observable x. It is, therefore, of great importance to have excellent detector resolutions in order to suppress the accidental background. Fig. 23 (a) shows the effective branching ratio for the accidental background as a function of the lower edges of E_e and E_γ of the signal region. The same plot for the physics background from RMD is shown in Fig. 23 (b), which is described in detail in the Sect. 4.2.2. It can be seen that the accidental background is much more severe than the physics background.

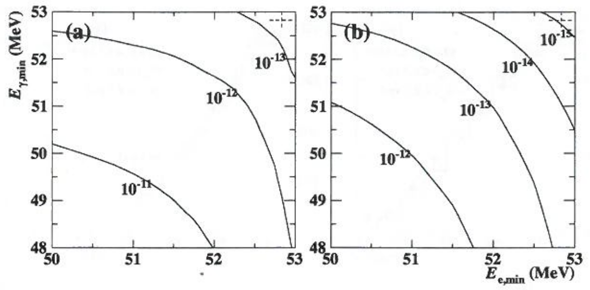

Figure 23 Effective branching ratios of the two types of background into kinematic window defined by $E_{e,\min} < E_e < 53.5$ MeV, $E_{\gamma,\min} < E_\gamma < 53.5$ MeV, $|t_{e\gamma}| < 0.24$ ns and $\cos\Theta_{e\gamma} < -0.9996$. (a) Accidental background evaluated from the timing side-band. (b) Physics background from $\mu^+ \to e^+\gamma\nu\bar{\nu}$ process calculated with theoretical formula folded with detector responses.

The rate of the accidental background expected in the analysis window was evaluated using the data ~~in~~ from a wider time window in the side-bands with larger statistics. The background rate measured in the side-bands is used as a statistical constraint in the likelihood analysis as described in Sect. 4.4. The distributions of the observables in the physics analysis were also precisely measured in the timing side-bands and used as the accidental background PDFs in the likelihood analysis.

4.3.3 Physics background (RMD)

Editor's comments:
Section coordinator: Yusuke

Another background source consists of the $\mu^+ \to e^+\gamma\nu\bar{\nu}$ RMD process, producing a time-coincident positron–γ-ray pair. The RMD events fall into the signal region when the two neutrinos carry away a small amount of momentum. On the other hand, observation of the RMD events provides a strong internal consistency check for the $\mu^+ \to e^+\gamma$ analysis.

~~We studied~~ The RMD in the E_γ side-band of the muon decay data defined by $43 < E_\gamma < 48$ MeV, $48 < E_e < 53$ MeV, $|\phi_{e\gamma}| < 0.3$ rad, and $|\theta_{e\gamma}| < 0.3$ rad was studied. The RMD events are identified by a peak around the centre in $t_{e\gamma}$ distribution (Fig. 18). The distribution of RMD in terms of energy and angle is measured by the fit to the $t_{e\gamma}$-distribution divided into energy and angle bins. Figure 24 shows the measured distributions. The rates and shapes are compared with the Standard Model calculation (in ~~the~~ lowest order) [27] and found to be consistent. The measured branching ratio within the energy side-band agrees with the calculation to within 5%.

The expected number of RMD events in the $\mu^+ \to e^+\gamma$ analysis window is calculated by extrapolating the energy side-band distribution to the analysis window, giving an estimate of $\langle N_{RMD}\rangle = 614 \pm 34$, which is used as a statistical constraint in the likelihood analysis.

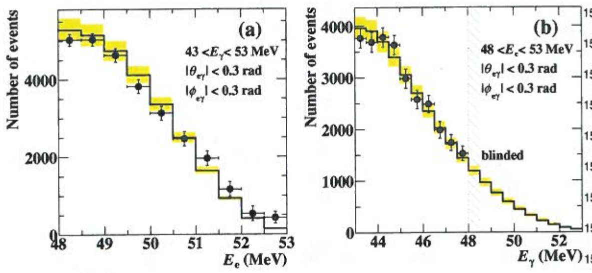

Figure 24 Projected distributions of $\mu^+ \to e^+\gamma\nu\bar{\nu}$ events measured in the energy side-band (dots with error bars) with the expectations (histograms with the uncertainty specified by the yellow bands). The expectations are calculated with the theoretical formula folded with the detector responses and a normalisation based on Michel events.

The RMD branching ratio is highly suppressed when the kinematic window ~~gets closer~~ is close to the limit of $\mu^+ \to e^+\gamma$ kinematics. The effective branching ratio, which is calculated by considering the detector resolution, is plotted in Fig. 23 (b) as a function of the lower limits of integration ranges on E_e and E_γ. For example, the effective branching ratio for $52.0 < E_\gamma < 53.5$ MeV and $52.0 < E_e < 53.5$ MeV is 3×10^{-14}, two orders of magnitude lower than that due to the accidental background.

4.4 Maximum likelihood analysis

Editor's comments:
Section coordinator: Fabrizio, Wataru, Ryu
Text: 2.
Figure: 4.

4.4.1 Maximum likelihood analysis

Editor's comments:
Section coordinator: Wataru

The numbers of signal, RMD and accidental background events in the analysis window ($48 < E_\gamma < 58$ MeV, $50 < E_e < 56$ MeV, $|t_{e\gamma}| < 0.7$ ns, $|\theta_{e\gamma}| < 50$ mrad and $|\phi_{e\gamma}| < 75$ mrad) are estimated by a maximum likelihood analysis with a likelihood function defined as

$$\mathcal{L}\left(N_{\rm sig}, N_{\rm RMD}, N_{\rm ACC}, \mathbf{t}\right) = \frac{e^{-N}}{N_{\rm obs}!} C(N_{\rm RMD}, N_{\rm ACC}, \mathbf{t}) \times \prod_{i=1}^{N_{\rm obs}} \left(N_{\rm sig} S(\mathbf{x}_i, \mathbf{t}) + N_{\rm RMD} R(\mathbf{x}_i) + N_{\rm ACC} A(\mathbf{x}_i)\right), \quad (2)$$

where $\mathbf{x_i} = \left\{E_\gamma, E_e, t_{e\gamma}, \theta_{e\gamma}, \phi_{e\gamma}\right\}$ is the vector of observables for the i-th event. $N_{\rm sig}$, $N_{\rm RMD}$ and $N_{\rm ACC}$ are the numbers of signal, RMD and accidental background events to be estimated, while S, R and A are their corresponding PDFs. $N = N_{\rm sig} + N_{\rm RMD} + N_{\rm ACC}$ and $N_{\rm obs}$ is the observed total number of events in the analysis window, $\mathbf{t}$ is a set of parameters which describe the position and the shape of the muon stopping target, C is a term for the constraints of nuisance parameters. The expected numbers of RMD and accidental background events with their respective uncertainties, which are evaluated in the side-bands, constitute Gaussian-constraints on $N_{\rm RMD}$ and $N_{\rm ACC}$ in the C term in Eq.2. The target position and shape parameters are prepared for each year. The fitting of the target positions is also constrained ~~with~~ by means of Gaussian functions whose sigmas are the uncertainty of the target position year by year. The uncertainty is 300 μm for 2009–2012 data, and 500 μm for 2013 data, respectively. The uncertainty of the target-shape due to ~~the~~ deformation is extracted from the difference between the shape measured with the FARO scan in 2013 and the fitted paraboloid (see Sect. 3.2.4). Since the deformation is likely to have ~~been~~ evolv~~ing~~ed, the larger shape-uncertainties are assigned for the later years; the maximum allowed deformations are 0.1, 0.1, 0.4, 0.5 and 1.0 of the measured FARO-paraboloid difference, for 2009-2013 data, respectively.

4.4.2 PDFs (Signal, BG)

Editor's comments:
Section coordinator: Ryu

4.4.2.1 Event-by-event PDFs

As the detector resolutions depend on the detector conditions and the hit-position in the detector, we have employed the method of using different PDFs for each event (event-by-event PDFs). The energy response, the position resolution and the background spectrum of the γ-ray detector are evaluated as a function of the impinging position and of the first conversion depth. For the PDF of the positrons, the fitting-errors of the tracking variables are used ~~for~~ to comput~~ing~~e the resolutions; namely a resolution (σ) is replaced by a product of a pull parameter (s) and the fitting-error (σ'). The pull parameter (s) for each observable is extracted from the data as described in Sect. 3.2.5. The pull parameters are common ~~for~~ to all events in a ~~certain~~ given DAQ period.

The correlations between observables are treated for each event. For example, because the emission angle of positrons is computed by extrapolating the fitted tracks to the target plane, the errors on the momentum and the angle are correlated. As the true positron momentum of the signal is known, the mean of the angle PDF can be corrected as a function of the observed momentum.

The PDFs of the observables (E_γ, E_e, $t_{e\gamma}$, $\theta_{e\gamma}$, $\phi_{e\gamma}$) for signal, RMD and accidental background events, respectively, are defined as

$$S\left(E_\gamma, E_e, t_{e\gamma}, \phi_{e\gamma}, \theta_{e\gamma} | \mathbf{p}_\gamma, \mathbf{p}_e, \sigma'_{E_e}, \sigma'_{\theta_e}, \sigma'_{\phi_e}, \sigma'_{\mathbf{p}_e}, \phi_e\right) =$$

$$
\begin{aligned}
& S(t_{e\gamma}|E_\gamma, E_e, \sigma'_{E_e}) \times \\
& S(\phi_{e\gamma}|\mathbf{p}_\gamma, \mathbf{p}_e, \theta_{e\gamma}, E_e, \sigma'_{E_e}, \sigma'_{\theta_e}, \sigma'_{\phi_e}, \sigma'_{\mathbf{p}_e}, \phi_e) \times \\
& S(\theta_{e\gamma}|\mathbf{p}_\gamma, \mathbf{p}_e, E_e, \sigma'_{E_e}, \sigma'_{\theta_e}, \sigma'_{\mathbf{p}_e}) \times \\
& S(E_e|\sigma'_{E_e}, \phi_e) \times \\
& S(E_\gamma|\mathbf{p}_\gamma), \qquad (3)
\end{aligned}
$$

$$
\begin{aligned}
R(E_\gamma, E_e, t_{e\gamma}, \phi_{e\gamma}, \theta_{e\gamma}|\mathbf{p}_\gamma, \mathbf{p}_e, \phi_e, \sigma'_{E_e}, \sigma'_{\theta_e}, \sigma'_{\phi_e}, \sigma'_{\mathbf{p}_e}) = {} & \\
& R(t_{e\gamma}|E_\gamma, E_e) \times \\
& R(E_\gamma, E_e, \phi_{e\gamma}, \theta_{e\gamma}|\mathbf{p}_\gamma, \mathbf{p}_e, \sigma'_{E_e}, \sigma'_{\theta_e}, \sigma'_{\phi_e}, \sigma'_{\mathbf{p}_e}, \phi_e), \qquad (4)
\end{aligned}
$$

$$
\begin{aligned}
A(E_\gamma, E_e, t_{e\gamma}, \phi_{e\gamma}, \theta_{e\gamma}|\mathbf{p}_\gamma, \mathbf{p}_e, \sigma'_{E_e}, \sigma'_{\theta_e}, \sigma'_{\phi_e}, \sigma'_{\mathbf{p}_e}, \phi_e) = {} & \\
& A(t_{e\gamma}) \times \\
& A(\phi_{e\gamma}|v_\gamma) \times \\
& A(\theta_{e\gamma}|u_\gamma) \times \\
& A(E_\gamma|\mathbf{p}_\gamma) \times \\
& A(E_e|\sigma'_{E_e}, \phi_e), \qquad (5)
\end{aligned}
$$

where $\mathbf{p}_\gamma$ and $\mathbf{p}_e$ is the first conversion point of the γ-ray and the muon decay vertex, respectively.

As the signal is a two-body decay, the signal PDFs are described by the detector resolutions. The PDFs for $\theta_{e\gamma}$ and $\phi_{e\gamma}$ are formed by combining the γ-ray position resolutions, the positron angle resolutions and the muon-decay position resolutions. The position resolutions of the γ-ray detector are evaluated from the MC simulation and validated in CEX experiments (see Sect. 3.1.3) The correlations between the errors of the observables are implemented in the $t_{e\gamma}$, $\theta_{e\gamma}$ and $\phi_{e\gamma}$ PDFs by shifting the centre and modifying the resolutions.

As ~~to~~ for the PDF for $t_{e\gamma}$, events are categorised by using the track-fitting quality and the matching quality between the fitted track and the hit-position on the timing counter. The resolution and the central value are extracted for each category from the observed RMD timing peak. The dependence on E_γ and E_e are taken into account. Most of the parameters used to describe the correlations are extracted from data by using the double-turn method (see Sect. 3.2.5), while a few parameters (the centre of the σ_{ϕ_e}–ϕ_e correlation, the slope parameter for the $\delta_{\phi_{e\gamma}}$–$\delta_{\theta_{e\gamma}}$ correlation and the slope parameter for the $\delta_{t_{e\gamma}}$–δ_{E_e} correlation, where δ_x is the difference between the observed and the true value of the observable x) are extracted from MC simulation. The energy response for monochromatic γ-rays is extracted ~~in the~~ from CEX runs as described in Sect. 3.1.3.

The RMD PDF is formed by ~~convolving~~ convolution of the detector response and the kinematic distribution of E_γ, E_e, $\theta_{e\gamma}$ and $\phi_{e\gamma}$ expected ~~in~~ from the Standard Model [27]. The correlations between the variables are included in the kinematic model. The PDF for $t_{e\gamma}$ is almost the same ~~as the one for~~ as that of the signal PDF, while the correlation between $\delta_{t_{e\gamma}}$ and E_e is ~~dropped~~ excluded.

The accidental background PDFs are extracted from the time side-band data. For E_e, the spectrum after applying the same event selection on the track-reconstruction quality as for the physics analysis is fitted with a function formed ~~from~~ by the convolution of the theoretical Michel positron spectrum and a parameterized function describing the detector response. For E_γ, the energy spectra after the application of the pile-up and cosmic ray cuts and of a loose selection on the γ–positron angle are fitted with a function to represent background γ-ray, remaining cosmic ray and the pile-up components ~~convolved~~ convoluted with the detector response. The $\theta_{e\gamma}$ and $\phi_{e\gamma}$ PDFs are represented ~~with~~ by polynomial functions fitted ~~on~~ to the data after applying the same event selection except for the $t_{e\gamma}$. For $t_{e\gamma}$, a flat PDF is used.

4.4.2.2 Constant PDFs

The event-by-event PDFs employ the ~~whole~~ total information we have about detector responses and kinematic variable correlations. A slightly less sensitive analysis, based on an alternative set of PDFs, is used as a cross check; this approach was already ~~followed~~ implemented in [6].

In this alternative set of PDFs the events are characterised by "categories", mainly determined by the tracking quality ~~for~~ of positrons and by the reconstructed depth of the first impinging point in the LXe detector for gamma rays. A constant group of PDFs is determined year by year, one for each of the categories mentioned above; the relative stereo angle $\Theta_{e\gamma}$ is ~~looked~~ searched for instead of $\theta_{e\gamma}$ and $\phi_{e\gamma}$ separately, while the three other kinematic variables (E_e, E_γ and $t_{e\gamma}$) are ~~in~~ common ~~between~~ to the two sets of PDFs. Correlations between kinematic variables are also taken into account in a more ~~simplified~~ simplistic way and the systematic uncertainties associated with the target position are included by shifting $\Theta_{e\gamma}$ of each event by an appropriate amount, computed by a combination of the corresponding shifts of $\theta_{e\gamma}$ and $\phi_{e\gamma}$. Signal and RMD PDFs are modelled as in the event-by-event analysis by using calibration data and theoretical distributions, folded with detector response; the likelihood function is analogous to Eq. 2 with the inclusion of the Gaussian constraints on the expected number of RMD and accidental background events and of the Poissonian constraint on the expected total number of events. In what follows we will refer to this set of PDFs as "constant PDFs" and to the analysis based on ~~that~~ it as "constant PDFs" analysis.

4.4.3 Confidence interval

Editor's comments:
Section coordinator: Ryu

The confidence interval of ~~the~~ N_{sig} is determined by the Feldman-Cousins approach [28] with the profile-likelihood ratio ordering [29]. For ordering experiments, the ratio of the likelihood at the best-fit and at given N_{sig} , which is defined

~~as~~ by the following equation, is used.

$$\lambda_p(N_{\rm sig}) = \begin{cases} \frac{\mathcal{L}(N_{\rm sig},\hat{\hat{\theta}}(N_{\rm sig}))}{\mathcal{L}(0,\hat{\hat{\theta}}(0))} & \text{if } \hat{N}_{\rm sig} < 0 \\ \frac{\mathcal{L}(N_{\rm sig},\hat{\hat{\theta}}(N_{\rm sig}))}{\mathcal{L}(\hat{N}_{\rm sig},\hat{\theta})} & \text{if } \hat{N}_{\rm sig} \geq 0, \end{cases} \tag{6}$$

where $\boldsymbol{\theta}$ is a vector of nuisance parameters ($N_{\rm ACC}$, $N_{\rm RMD}$ and target position and shape parameters), $\hat{N}_{\rm sig}$ and $\hat{\boldsymbol{\theta}}$ are the values of $N_{\rm sig}$ and $\boldsymbol{\theta}$ which maximize the likelihood, $\hat{\hat{\boldsymbol{\theta}}}(N_{\rm sig})$ is the value of $\boldsymbol{\theta}$ which maximizes the likelihood for the specified $N_{\rm sig}$. The confidence interval is calculated using the distribution of the likelihood-ratio in an ensemble of MC simulations. The following systematic uncertainties are included in the confidence interval; the normalisation (defined in Sect. 4.5), the alignment of the gamma and the positron detectors, the alignment (position and shape) of the muon stopping target, the gamma-energy scale, the positron energy bias, the centre of the signal $t_{e\gamma}$ PDF, shapes of the signal and background PDFs and the correlations between the errors of the positron observables. The dominant systematic uncertainty is due to the target alignment as described in Sect. 4.6.1, which ~~is~~ include~~d~~s ~~by~~ profiling it within the likelihood fitting. Other uncertainties are included by randomising them in the generation of the MC simulations used to construct the distribution of the likelihood-ratio.

4.5 Normalisation

Editor's comments:
Section coordinator: Yusuke, Luca
Text: 1.
Figure: 1.

The normalisation factor N_μ is the number of muon decays effectively measured during the experiment and is used to express the branching ratio in terms of the number of signal events ($N_{\rm sig}$)

$$\mathcal{B}(\mu^+ \to {\rm e}^+\gamma) \equiv \frac{\Gamma(\mu^+ \to {\rm e}^+\gamma)}{\Gamma_{\rm total}} = \frac{N_{\rm sig}}{N_\mu}.$$

Two independent methods are used to calculate N_μ. Since both methods use control samples measured simultaneously with a signal, they are independent of the instantaneous beam rate.

4.5.1 Michel positron counting

Editor's comments:
Section coordinator: Daisuke

The number of high momentum Michel positrons is counted using a pre-scaled TC based trigger enabled during the physics data taking. Since $\mathcal{B}(\mu^+ \to {\rm e}^+\nu\bar{\nu}) \approx 1$, N_μ is calculated as follows,

$$N_\mu = \frac{N^{{\rm e}\nu\bar{\nu}}}{f_E^{{\rm e}\nu\bar{\nu}}} \times \frac{P^{{\rm e}\nu\bar{\nu}}}{\epsilon_{\rm trg}^{{\rm e}\nu\bar{\nu}}} \times \frac{\epsilon_{\rm e}^{{\rm e}\gamma}}{\epsilon_{\rm e}^{{\rm e}\nu\bar{\nu}}} \times A_\gamma^{{\rm e}\gamma} \times \epsilon_\gamma^{{\rm e}\gamma} \times \epsilon_{\rm trg}^{{\rm e}\gamma} \times \epsilon_{\rm sel}^{{\rm e}\gamma},$$

where $N^{{\rm e}\nu\bar{\nu}} = 245\,860$ is the number of Michel positrons detected in $50 < E_{\rm e} < 56$ MeV; $f_{E_{\rm e}}^{{\rm e}\nu\bar{\nu}} = 0.101 \pm 0.001$ is the fraction of Michel spectrum for this energy range (the uncertainty coming from the systematic uncertainty on the $E_{\rm e}$ bias); $P^{{\rm e}\nu\bar{\nu}} = 10^7$ is the pre-scaling factor of the Michel positron trigger, which requires a correction factor $\epsilon_{\rm trg}^{{\rm e}\nu\bar{\nu}} = 0.894 \pm 0.009$ to account for the dead time of the trigger scaler due to pile-up in the TC; $\epsilon_{\rm e}^{{\rm e}\gamma}/\epsilon_{\rm e}^{{\rm e}\nu\bar{\nu}}$ is the ratio of signal-to-Michel efficiency for detection of positrons in this energy range; $A_\gamma^{{\rm e}\gamma} = 0.985 \pm 0.005$ is the geometrical acceptance for signal γ-ray given an accepted signal positron; $\epsilon_\gamma^{{\rm e}\gamma}$ is the efficiency for detection and reconstruction of 52.83 MeV γ-rays; $\epsilon_{\rm trg}^{{\rm e}\gamma}$ is the trigger efficiency for signal events; and $\epsilon_{\rm sel}^{{\rm e}\gamma}$ is the e$^+$–γ pair selection efficiency for signal events given a reconstructed positron and a γ-ray.

The absolute values of positron acceptance and efficiency ~~are cancelled out~~ cancel in the ratio $\epsilon_{\rm e}^{{\rm e}\gamma}/\epsilon_{\rm e}^{{\rm e}\nu\bar{\nu}}$. Small momentum dependent effects are ~~extracted~~ derived from the Michel spectrum fit, resulting in $\epsilon_{\rm e}^{{\rm e}\gamma}/\epsilon_{\rm e}^{{\rm e}\nu\bar{\nu}} = 1.149 \pm 0.017$.

The γ-ray efficiency is evaluated via the MC simulation taking into account the observed event distribution. The average value is $\epsilon_\gamma^{{\rm e}\gamma} = 0.647$. The main contribution to the γ-ray inefficiency is from conversions before the LXe active volume: 14% loss in the COBRA magnet, 7% in the cryostat and PMTs, and 7% in other materials. Another loss is due to shower escape from the inner face, resulting in a 6% loss. The γ-ray efficiency is also measured in the CEX run. By tagging an 83-MeV γ-ray from a π^0 decay, the efficiency for detection of 55-MeV γ-rays is measured to be 0.64–0.67, consistent with the evaluation from MC simulations. With an additional selection efficiency of 0.97 resulting ~~by~~ from the rejection of pile-up and cosmic ray events, $\epsilon_\gamma^{{\rm e}\gamma} = 0.625 \pm 0.023$.

The trigger efficiency consists of three components; γ-ray energy, time coincidence, and direction match. The efficiency of γ-ray energy is estimated from the online energy resolution and found to be $\gtrsim 0.995$ for $E_\gamma > 48$ MeV. The timing efficiency is also estimated from the online time resolution and is found to be fully efficient. The directional match efficiency is evaluated, based on the MC simulation, to be $\epsilon_{\rm trg}^{{\rm e}\gamma} = 0.91 \pm 0.01$ and 0.96 ± 0.01 for the data before and after 2011, respectively (Fig. 9).

~~On~~ From e$^+$–γ pairs, which satisfy the selection criteria for each particle, two kinds of further selection are imposed. One is the cut for the AIF-like events described in Sect. 3.2.8, resulting in 1.1% inefficiency for the signal events. The other is defined by the analysis window, in particular that for the relative angles and timing. The inefficiency is evaluated via the MC simulation taking into account the pile-up and detector condition. A loss of 3.2% comes from the tails in the angular responses. Additionally, about 1.5% of events are outside the time window, mainly due to the erroneous reconstruction of the positron trajectory where one of the turns, usually the first, is missed. As a result, $\epsilon_{\rm sel}^{{\rm e}\gamma} = 0.943 \pm 0.010$.

In total, the Michel positron counting method provides N_μ with a 4.5% uncertainty.

4.5.2 RMD channel

Editor's comments:
Section coordinator: Yusuke

The other method uses RMD events detected in the $\mu^+ \to e^+\gamma$ trigger data. ~~Similarly to~~ As for the Michel method, N_μ is expressed as,

$$N_\mu = \frac{N^{e\nu\bar{\nu}\gamma}}{\mathcal{B}^{e\nu\bar{\nu}\gamma}} \times \frac{\epsilon_e^{e\gamma}}{\epsilon_e^{e\nu\bar{\nu}\gamma}} \times \frac{\epsilon_\gamma^{e\gamma}}{\epsilon_\gamma^{e\nu\bar{\nu}\gamma}} \times \frac{\epsilon_{\mathrm{trg}}^{e\gamma}}{\epsilon_{\mathrm{trg}}^{e\nu\bar{\nu}\gamma}} \times \frac{\epsilon_{\mathrm{sel}}^{e\gamma}}{\epsilon_{\mathrm{sel}}^{e\nu\bar{\nu}\gamma}},$$

where $\mathcal{B}^{e\nu\bar{\nu}\gamma}$ is the partial branching ratio of RMD in the relevant kinematic range, and the other factors are defined in the same way as for the Michel case. ~~Since~~ As the same data sample is used and the γ-ray is also detected in this mode, all the efficiency factors are expressed in signal-to-RMD ratios. ~~On the other hand~~ In contrast, the efficiency ratios need to be evaluated differentially as functions of the relevant kinematic variables because the kinematic range is wider than the $\mu^+ \to e^+\gamma$ analysis window.

We use events reconstructed in the E_γ side-band defined in Sect. 4.3.3, corresponding to $\mathcal{B}^{e\nu\bar{\nu}\gamma} = 4.9 \times 10^{-9}$. The number of RMD events is extracted from the fit to the $t_{e\gamma}$ distribution separately for each year data sample and for 12 statistically independent sub-windows, resulting in $N^{e\nu\bar{\nu}\gamma} = 29\,950 \pm 527$ in total.

The momentum dependent ratio of the positron detection efficiency is extracted from the Michel spectrum fit. An additional correction for the momentum dependence of the missing turn probability is applied based on the evaluation ~~with~~ of the MC simulation. A pre-scaled trigger with a lowered E_γ threshold (by ~ 4 MeV) allows for a relative measurement of the energy-dependent efficiency curve of the LXe detector. The efficiency ratio of the direction match is evaluated from the distribution of accidental background. The effect of muon polarisation [30], which makes the background distribution non-flat (asymmetric) even in case of a detector and trigger fully efficient, ~~is taken into account~~. Inefficiency due to the AIF-like events cuts and the tail in the time reconstruction are common to signal and RMD, and thus, only tails in the angular responses are relevant. A more detailed description of the RMD analysis is found in [31].

A χ^2 fit is performed to extract N_μ from the measured RMD spectrum. The systematic uncertainty on each factor, correlated among different windows, is inserted in the χ^2 as a pull term. The uncertainty on N_μ from the fit to the full data sample is 5.5%.

4.5.3 N_μ summary

The normalisation factors calculated by the two methods are shown in Fig. 25. The two independent results are in good agreement and combined to give N_μ with a 3.5% uncertainty. The single event sensitivity for the full data sample is $1/N_\mu = (5.84 \pm 0.21) \times 10^{-14}$.

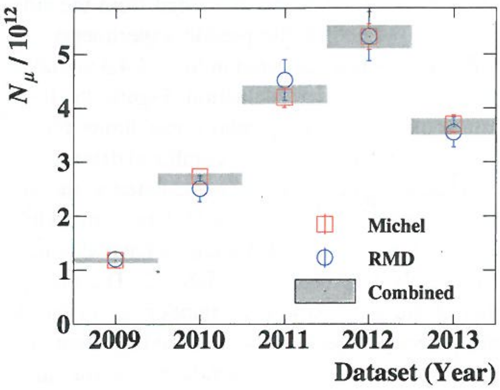

Figure 25 N_μ calculated with the two methods and the combination for each year dataset.

The normalisation factor can also be expressed by

$$N_\mu = N_\mu^{\mathrm{stop}} \cdot \Omega \cdot \epsilon,$$

where N_μ^{stop} is the total number of muons stopped in the target, Ω is the geometrical acceptance of the apparatus and ϵ is the overall efficiency. The integration of the estimated stopping rate, corrected for by the variation of the primary proton beam current, over the live time gives an estimate of $N_\mu^{\mathrm{stop}} \approx 7.5 \times 10^{14}$ (Fig. 20). Therefore, ~~we get~~ an estimate of the overall signal acceptance of $\sim 2.3\%$ is obtained. This is consistent with $\Omega \approx 0.11$ and our estimates of detector efficiencies, $\epsilon_e \cdot \epsilon_\gamma \sim 0.30 \times 0.63$.

4.6 Results

Editor's comments:
Section coordinator: Fabrizio, Wataru, Ryu, Daisuke
Text: 3.
Figure: 5.

A maximum likelihood analysis has been performed to extract the number of signal events ~~in~~ from the full dataset after the analysis tools were fully optimised and background studies in the side-bands were completed. The sensitivity and the results in the analysis window are presented and discussed in the following sections.

4.6.1 Sensitivity

The sensitivity of the analysis is evaluated by taking the median average of the distribution of the branching ratio upper limits at 90% C.L. observed for an ensemble of pseudo experiments with a null signal hypothesis. The rates of RMD and accidental background events estimated from the side-band studies are assumed in the pseudo experiments. All the systematic uncertainties as listed in Sect. 4.4.3 are taken into account in the sensitivity evaluation. Figure 26 shows the distribution of the branching ratio upper limits for the pseudo experiments simulated for the combined dataset. The sensitivity ~~for~~ of the combined dataset is calculated as the median of the distribution and found to be 5.6×10^{-13}. The sensitivities for the 2009–2011 and 2012–2013 datasets have also been evaluated separately as presented in Table 2. The average contributions of the systematic uncertainties are evaluated by calculating the sensitivities without including them. The dominant one is found to be the uncertainty on the target alignment; it degrades the sensitivity by 18% on average, while the total contribution of the other systematic uncertainties is less than 1%. The sensitivity for the 2009–2011 dataset is found to be slightly worse than previously quoted in [6] due to a more conservative assignment of the systematic uncertainty on the target alignment. The likelihood analysis has also been tested in fictitious analysis windows in $t_{e\gamma}$-side-bands centred at $t_{e\gamma} = \pm 2$ ns without the Gaussian constraint on N_{RMD} in the likelihood analysis. The upper limit observed in the negative and positive time side-band is 8.4×10^{-13} and 8.3×10^{-13}, respectively. ~~They~~ These are consistent with the upper limit distribution for pseudo experiments as indicated in Fig.26.

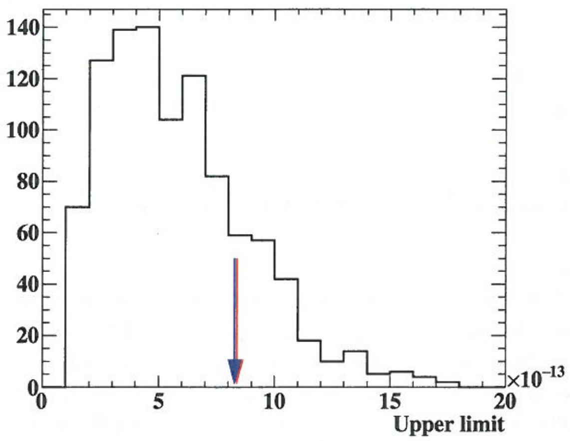

Figure 26 Distribution of the branching ratio upper limits for pseudo experiments simulated for the full dataset. The sensitivity is calculated as the median average of the distribution to be 5.6×10^{-13}. The upper limits observed in the $t_{e\gamma}$-side-bands are indicated with arrows for comparison. ~~Two~~ The two arrows overlap as the observed upper limits are almost the same ~~accidentally~~.

4.6.2 Likelihood analysis in signal region

Figure 27 shows the event distributions for the 2009-2013 combined dataset on the (E_e-E_γ)- and ($\cos\Theta_{e\gamma}$-$t_{e\gamma}$)-planes respectively, where $\Theta_{e\gamma}$ is the opening angle between positron and γ-ray. The contours of the averaged signal PDFs are also shown for comparison. No significant correlated excess is observed within the signal contours.

! Since one see events in both 1σ regions but not correlated!

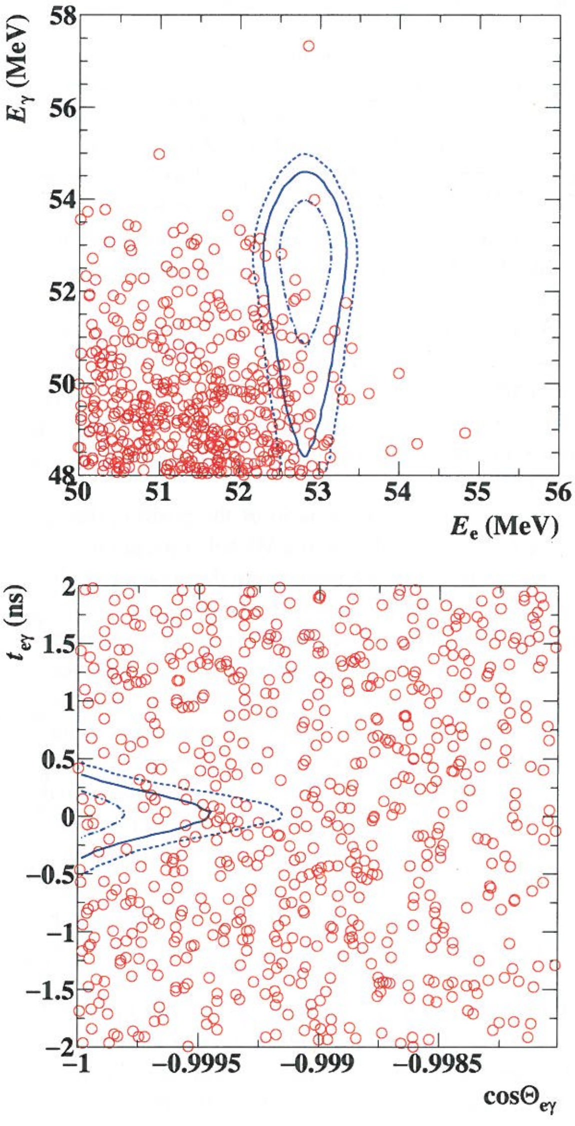

Figure 27 Event distributions of observed events in the ($E_e - E_\gamma$)- and ($\cos\Theta_{e\gamma} - t_{e\gamma}$)-planes. In the top figure, selections of $\cos\Theta_{e\gamma} < -0.99963$ and $|t_{e\gamma}| < 2.4$ ns are applied with 90% efficiency for each variable, and in the bottom ~~one~~ figure $51.0 < E_\gamma < 55.5$ MeV and $52.4 < E_e < 55.0$ MeV are applied with 74% and 90% efficiency respectively. The signal PDF contours (1σ, 1.64σ and 2σ) are also shown.

Table 2 Best fit values ($\mathcal{B}_{\mathrm{fit}}$'s), branching ratios ($\mathcal{B}_{90}$) and sensitivities ($S_{90}$)

dataset	2009–2011	2012–2013	2009-2013
$\mathcal{B}_{\mathrm{fit}} \times 10^{13}$	−1.3	−5.5	−2.3
$\mathcal{B}_{90} \times 10^{13}$	6.1	7.9	4.2
$S_{90} \times 10^{13}$	8.0	8.3	5.6

A maximum likelihood analysis has been performed to evaluate the number of signal events in the analysis window by the method described in Sect. 4.4. Figure 28 shows the profile likelihood ratios as a function of the branching ratio observed for 2009–2011, 2012–2013, and 2009–2013 combined dataset, which are all consistent with a ~~the~~ signal hypothesis. The kinks seen in the curves (most obvious in 2012–2013) are due to the fitting ~~on~~ of target local parameters (Sect.4.4.1). On ~~In~~ the negative and positive side of branching ratio, the local parameters are fitted to opposite sides, therefore the likelihood curve shifts from one to another around 0 in branching ratio. The best fit and the upper limit (90% C.L.) on the branching ratio for the combined dataset are -2.3×10^{-13} and 4.2×10^{-13}, respectively. The results from the likelihood analysis are summarized in Table 2. The dominant systematic uncertainty is due to the target alignment uncertainty, which increases the upper limit by 5% while the other uncertainties increase it by less than 1% in total.

The upper limit on the branching ratio is consistent with the sensitivity under the background-only hypothesis presented in Sect.4.6.1. This result was confirmed by following the profile of the log-likelihood curve as a function of the number of signal events, in parabolic approximation, and by an independent analysis, based on a set of constant PDFs, which will be discussed in Sect. 4.6.3.

The projection of the best fitted function on each observable is shown in Fig. 29. (a)–(e), where all the fitted spectra are in good agreement with the data spectra. The agreement is also confirmed by ~~with~~ the relative signal likelihood R_{sig} defined as,

$$R_{\mathrm{sig}} = \ln\left(\frac{S(\mathbf{x}_i)}{f_R R(\mathbf{x}_i) + f_A A(\mathbf{x}_i)}\right), \tag{7}$$

where S, R, A are the PDFs for signal, RMD and accidental background, respectively for the i-th event with observables $\mathbf{x}_i$. f_R and f_A are the approximate fractions of the RMD and accidental background events which are estimated to be 0.1 and 0.9 in the side-bands, respectively. Figure 29 (f) shows the R_{sig} distribution observed in the combined dataset together with the expected distribution from the fit result.

A maximum likelihood fit without the constraints on N_{RMD} and N_{ACC} estimated from the side-bands has been performed as a consistency check. The best fit values of N_{RMD} and N_{ACC} for the combined dataset are 7684 ± 103 and 663 ± 59, respectively. They are consistent with the respective expectations of 7744 ± 41 and 614 ± 34 and also with the total number of the observed events ($N_{\mathrm{obs}} = 8344$) in the analysis window.

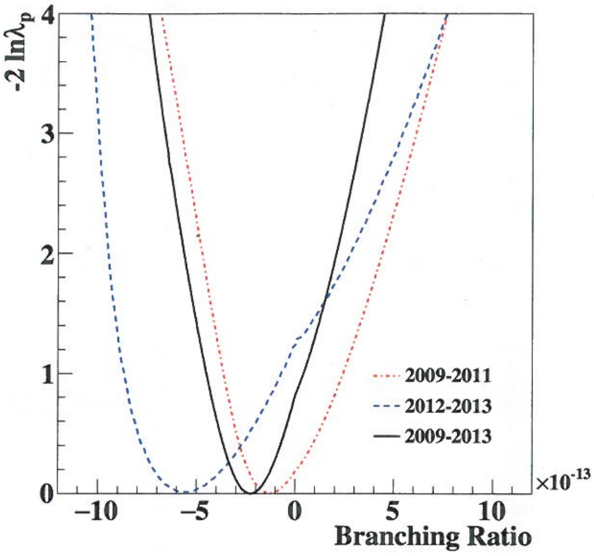

Figure 28 The negative log likelihood ratio (λ_p) as a function of branching ratio.

4.6.3 Discussions

A maximum likelihood fit was also performed by using the constant PDFs, obtaining results in good agreement with those of the analysis based on event-by-event PDFs. The best fit and upper limit at 90% C.L. on the branching ratio obtained by this analysis on the full dataset are -2.5×10^{-13} and 4.3×10^{-13} respectively, in close agreement with the results of the event-by-event PDF analysis presented in Sect. 4.6.2. The fitted values of RMD and accidental events are 630 ± 66 and 7927 ± 148, in agreement with the expected values obtained by extrapolations from the side-bands of 683 ± 115 and 7915 ± 96. These numbers also agree with ~~that~~ those of the event-by-event analysis when one takes into account that the angular selection based on the relative stereo angle ($\Theta_{e\gamma} > 176°$) selects $\approx 3\%$ more accidental events than that based on $\theta_{e\gamma}$ and $\phi_{e\gamma}$. Fig. 30 shows ~~As~~ an example of the results obtained with the constant PDFs after analysis ~~we show in Fig. 30~~ the projection of the best fitted function on $\Theta_{e\gamma}$: the fitted and the data distributions are in good agreement.

The consistency ~~between~~ of the two analyses was also checked by ~~on~~ a set of pseudo experiments, specifically produced to be compatible with the structures of both the analyses ("common toy MCs"). The upper limits at 90% C.L. observed in the two analyses for a sample of several hundred common toy MCs are compared in Fig. 31; the experimental result is

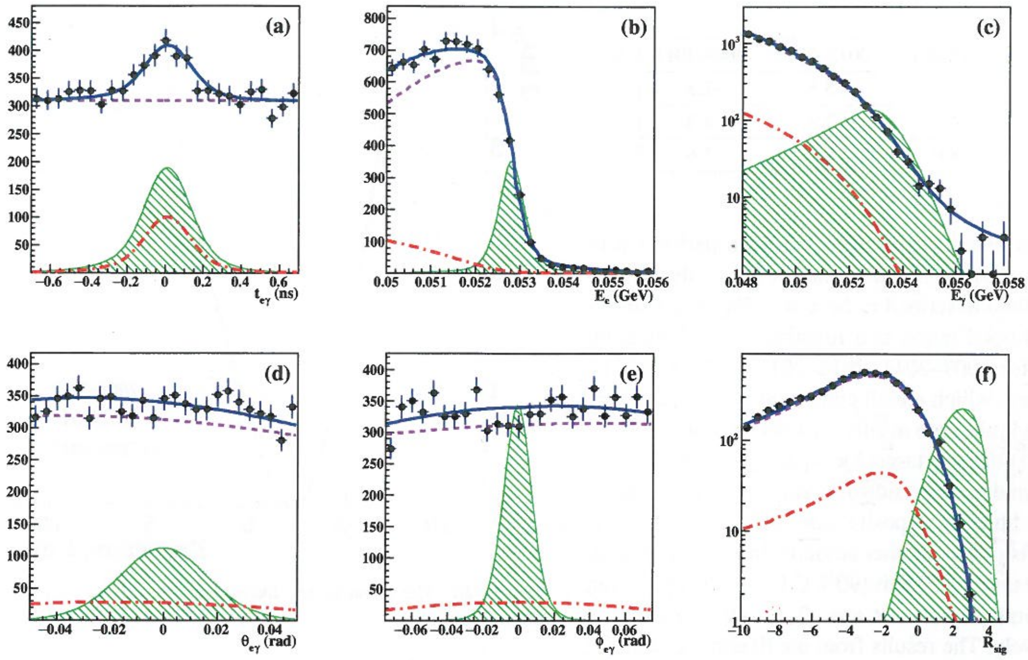

Figure 29 The projections of the best fitted likelihood function to the five main observables and $R_{\rm sig}$. The markers show the 2009–2013 combined data. The magenta dash and red dot-dash lines are individual components of the fitted PDFs of ACC and RMD, respectively. The blue solid line is the sum of the best fitted PDFs. The green hatched histograms show the signal PDFs corresponding to 100 times magnified $N_{\rm sig}$ upper limit.

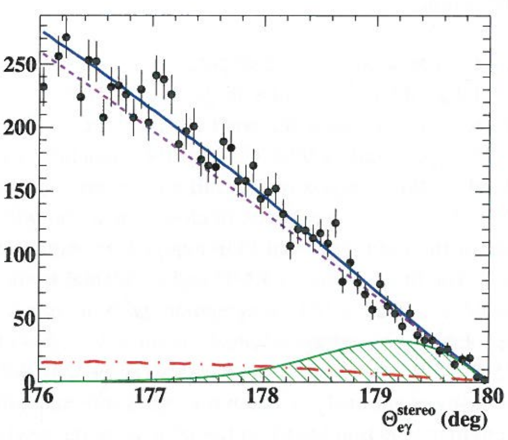

Figure 30 The distribution of the relative stereo angle $\Theta_{e\gamma}$ obtained in the constant PDF analysis for experimental data (black dots) and the fitted spectrum. The RMD and accidental background components and their sum are in red, magenta and blue respectively; the green hatched histogram shows the signal PDF corresponding to 100 times magnified $N_{\rm sig}$ upper limit.

by (black) !

marked ~~with~~ a ~~red~~ star. The upper limits for the two analyses are well correlated and the analysis based on event-by-event PDFs shows ~ 20% better sensitivity. By analysing the distribution of the differences between the UL reconstructed by the two analyses on this sample of common toy MCs we found that the probability of ~~getting~~ obtaining a difference in the upper limit at least equal to that measured on the real data is 70%.

The previous MEG publication [6] reported on the analysis based on the 2009–2011 dataset. The analysis presented here includes a re-analysis of the 2009-2011 dataset with improved algorithms. Since the analysis algorithms are revised, the reconstructed observables are slightly changed, ~~though~~ albeit within the detector resolutions. A change in the result of the likelihood analysis is expected due to statistical effects. The expected difference in the upper limit between the old and new analyses for the 2009–2011 dataset was evaluated by a set of toy MC simulations based on the expected changes in the reconstructed observables, ~~showing~~ and shows a spread of $\Delta\mathcal{B} = 4.2 \times 10^{-13}$ (RMS) with a mean of nearly zero. The difference observed in the experimental data is $\Delta\mathcal{B} = 0.4 \times 10^{-13}$ and lies well within the spread.

5 Conclusions

Section coordinator: Paolo
Text: 1.
Figure: 0.

A high-precision search for the lepton flavour violating muon decay mode $\mu^+ \to e^+\gamma$ ~~has been~~ was performed with the

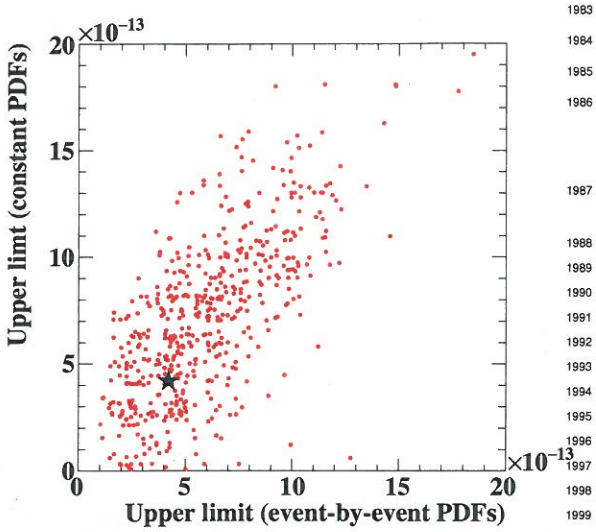

Figure 31 The comparison of the 90 % C.L. upper limits reconstructed on a sample of several hundred common toy MCs by the constant PDF and the event-by-event PDF based analyses. The upper limits observed in the experimental data are marked ~~with~~ by a ~~red~~ Black star. The two analyses look well compatible, with a ~ 20% better sensitivity on average for that based on event-by-event PDFs.

MEG detector in the years 2009–2013. A blind maximum likelihood analysis ~~establishes~~ established a new upper limit for the branching ratio of $\mathcal{B}(\mu^+ \to e^+\gamma) < 4.2 \times 10^{-13}$ with 90% confidence. This upper limit is the most stringent ~~up~~ to date and provides important constraints on the existence of physics beyond the Standard Model.

The new measured upper limit improves our previous result [6] by a factor 1.4; the improvement in sensitivity is also ~~a~~ far from the amounts to factor 1.4. Compared with the limit previous ~~to~~ MEG [32], our new upper limit represents ~~an~~ significant improvement ~~by~~ a factor collaboration that of a 30.

At present ~~An~~ an effort ~~is ongoing~~ is underway to upgrade the existing ~~apparatus~~ MEG detector to achieve an additional improvement in the sensitivity ~~to~~ of the $\mathcal{B}(\mu^+ \to e^+\gamma)$ [33]: with a goal the tracking and timing detectors for measuring the positrons have in the mean time been completely redesigned, while other parts of the detector have been refurbished. The new ~~apparatus~~ ly designed experiment, MEG II, will be able to cope with a muon decay rate on target twice as large as that of MEG. The improved detector is expected to bring the branching ratio sensitivity down to 5×10^{-14} with three years of data taking planned for in the ~~next~~ coming years.

Acknowledgments

We are grateful for the support and co-operation provided by PSI as the host laboratory and to the technical and engineering staff of our institutes. This work is supported by DOE DEFG02-91ER40679 (USA), INFN (Italy), MEXT KAKENHI 22000004 and 26000004 (Japan), Schweizerischer Nationalfonds (SNF) Grant 200021_137738, the Russian Federation Ministry of Education and Science and Russian Fund for Basic Research grant RFBR-14-22-03071.

References

1. R. Barbieri, L. Hall, A. Strumia, Violations of lepton flavour and CP in supersymmetric unified theories. Nucl. Phys. B **445**(2–3), 219–251 (1995). doi:10.1016/0550-3213(95)00208-A
2. S. Mihara et al., Charged Lepton Flavor-Violation Experiments. Ann. Rev. Nucl. Part. Sci. **63**, 531–552 (2013). doi:10.1146/annurev-nucl-102912-144530
3. Y. Hisamatsu, Search for the lepton flavour-violating decay $\mu^+ \to e^+\gamma$. Eur. Phys. J. C **52**, 477–485 (2007). doi:10.1140/epjc/s10052-007-0383-7
4. J. Adam et al. (MEG Collaboration), A limit for the $\mu \to e\gamma$ decay from the MEG experiment. Nucl. Phys. **B834**, 1–12 (2010). doi:10.1016/j.nuclphysb.2010.03.030, arXiv:0908.2594
5. J. Adam et al. (MEG Collaboration), New limit on the lepton-flavor violating decay $\mu^+ \to e^+\gamma$. Phys. Rev. Lett. **107**, 171801 (2011). doi:10.1103/PhysRevLett.107.171801, arXiv:1107.5547
6. J. Adam et al. (MEG Collaboration), New constraint on the existence of the $\mu^+ \to e^+\gamma$ decay. Phys. Rev. Lett. **110**, 201801 (2013). doi:10.1103/PhysRevLett.110.201801, arXiv:1303.0754
7. J. Adam et al., The MEG detector for $\mu^+ \to e^+\gamma$ decay search. Eur. Phys. J. C **73**, 2365 (2013). doi:10.1140/epjc/s10052-013-2365-2, arXiv:1303.2348
8. W. Ootani et al., Development of a thin-wall superconducting magnet for the positron spectrometer in the MEG experiment. IEEE Trans. Appl. Supercond. **14**(2), 568–571 (2004). doi:10.1109/TASC.2004.829721
9. C. de Boor. *A Practical Guide to Splines*. Springer (1978)
10. M. Hildebrandt, The drift chamber system of the MEG experiment. Nucl. Instrm. and Meth. A **623**(1), 111–113 (2010). doi:10.1016/j.nima.2010.02.165
11. S. Dussoni et al., The Timing Counter of the MEG experiment: design and commissioning. Nucl. Instrm. and Meth. A **617**(1-3), 387–390 (2010). doi:10.1016/j.nima.2009.08.089
12. M. De Gerone et al., Development and commissioning of the Timing Counter for the MEG Experiment. IEEE Trans. Nucl. Sci. **59**, 379–388 (2012). doi:10.1109/TNS.2012.2187311, arXiv:1112.0110
13. M. De Gerone et al., The MEG timing counter calibration and performance. Nucl. Instrm. and Meth. A **638**, 41–46 (2011). doi:10.1016/j.nima.2011.02.044
14. R. Sawada, Performance of liquid xenon gamma ray detector for MEG. Nucl. Instrm. and Meth. A **623**(1), 258–260 (2010). doi:10.1016/j.nima.2010.02.214
15. A. Baldini et al., A radioactive point-source lattice for calibrating and monitoring the liquid xenon calorimeter of the MEG experiment. Nucl. Instrm. and Meth. A **565**(2), 589–598 (2006). doi:10.1016/j.nima.2006.06.055
16. J. Adam et al. (MEG Collaboration), Calibration and monitoring of the MEG experiment by a proton beam from a Cockcroft–Walton accelerator. Nucl. Instrm. and Meth. A **641**, 19–32 (2011). doi:10.1016/j.nima.2011.03.048
17. G. Rutar et al., A dedicated calibration tool for the MEG and MEG II positron spectrometer. Nucl. Instrm. and Meth. A (In print). doi:10.1016/j.nima.2015.11.121
18. S. Ritt, R. Dinapoli, U. Hartmann, Application of the DRS chip for fast waveform digitizing. Nucl. Instrm. and Meth. A **623**(1), 486–488 (2010). doi:10.1016/j.nima.2010.03.045